Comparison of Laser Ion Acceleration from the Front and Rear Surfaces of Thin Foils

J. Fuchs,[1,2,6] Y. Sentoku,[1,6] S. Karsch,[3] J. Cobble,[4] P. Audebert,[2] A. Kemp,[1,6] A. Nikroo,[1] P. Antici,[2] E. Brambrink,[5]
A. Blazevic,[5] E. M. Campbell,[1] J. C. Fernández,[4] J.-C. Gauthier,[2] M. Geissel,[5] M. Hegelich,[3,4] H. Pépin,[2] H. Popescu,[2]
N. Renard-LeGalloudec,[6] M. Roth,[5] J. Schreiber,[3] R. Stephens,[1] and T. E. Cowan[1,6]

[1]*General Atomics, San Diego, California 92121, USA*
[2]*Laboratoire pour l'Utilisation des Lasers Intenses, UMR 7605 CNRS-CEA-École Polytechnique-Univ. Paris VI, Palaiseau, France*
[3]*Max-Planck-Institut für Quantenoptik, 85748 Garching, Germany*
[4]*University of California, Los Alamos National Laboratory, Los Alamos, New Mexico 87545, USA*
[5]*Technische Univ. Darmstadt, 64289 Darmstadt, Germany*
[6]*Physics Department, MS-220, University of Nevada, Reno, Nevada 89557, USA*

(Received 11 March 2004; published 3 February 2005)

The comparative efficiency and beam characteristics of high-energy ions generated by high-intensity short-pulse lasers ($\sim$1–6 $\times$ 10^{19} W/cm^2) from both the front and rear surfaces of thin metal foils have been measured under identical conditions. Using direct beam measurements and nuclear activation techniques, we find that rear-surface acceleration produces higher energy particles with smaller divergence and a higher efficiency than front-surface acceleration. Our observations are well reproduced by realistic particle-in-cell simulations, and we predict optimal criteria for future applications.

DOI: 10.1103/PhysRevLett.94.045004 PACS numbers: 52.38.Kd, 07.77.Ka, 24.10.Lx, 52.70.Nc

Recent observations of intense beams of multi-MeV protons generated by intense short-pulse lasers irradiating thin solid foils [1,2] have opened perspectives for important applications like high-brightness ion sources [3], radioisotope generators [4], proton radiography [5,6], or high-energy density matter [7]. There is, however, still a controversy regarding the origin of the accelerated protons, a matter of crucial importance in the prospect of properly optimizing the ion beam properties for any particular application.

There are two main mechanisms that lead to laser acceleration of high-energy protons in the forward direction. First, at the laser-irradiated target surface, the laser pressure sets an electric field which sweeps electrons from the interaction region and induces front-surface acceleration (FSA) of ions into and through the target [8]. Second, at the nonirradiated rear surface, fast electrons that have propagated through the target form a dense sheath. The rear-surface acceleration (RSA) $\sim$TV/m electric field ionizes atoms and accelerates ions normal to the surface [2,9]. For both mechanisms, accelerated protons stem either from contaminants (e.g., water vapor) present on all target surfaces, or from prepared layers. Theoretical studies [8,10] predict that RSA produces higher energy ions with a higher conversion efficiency than FSA.

At low laser energy, it has been shown in spherical targets [11] that RSA was predominant. At high laser energy ($>$1 J), two experiments concluded incorrectly that the highest energy protons originate from FSA [12,13]. In Ref. [12], this conclusion is based on the observation of a ring structure on the detector (CR-39) which is clearly visible only when a thick 20 μm hydrogenous (PEEK) layer is on the front surface of a heated Al substrate. From unheated targets shots, the ring structure is attributed to high-energy protons. However, the ring structure arises most likely from saturation effects in CR-39 at high proton fluences and is not a signature of high-energy protons. The differences in the proton fluence, and hence in the observation or not of the ring, between the cases where the PEEK layer is at the front or the rear are essentially related to changes in the hot electron source (preplasma conditions) and to the peculiarity of hot electron transport in a thick insulating layer [14]. Regarding Ref. [13], we believe that the rear surface of the 6 μm Mylar foil used in this experiment was preheated by the laser amplified spontaneous emission, i.e., ASE ($\sim 10^{13}$ W cm^{-2} at $\lambda_0 = 1$ μm). In such a case, a sharp gradient at the rear surface does not exist anymore and RSA cannot take place [15]. We have checked this experimentally and through simulations.

In this Letter, we present the first direct and quantitative comparison of RSA and FSA under identical laser conditions. On two different high-energy laser facilities, we not only observe, for thin targets, predominance of RSA over FSA at high proton energies, in sharp contrast with Refs. [12,13], but we also determine quantitatively the respective contributions of RSA and FSA for high-energy protons. Under our laser conditions ($\sim$20–30 J) and for thin (20 μm) metal foils, RSA produces a collimated ($\leq 20^\circ$) beam of energetic protons $>$16 MeV while FSA produces a high-divergence, low-energy ($\leq$6 MeV) beam. We find that for protons $>$3.5 MeV, FSA accounts for $<$3% of the total energy of the accelerated protons. When the target thickness is increased, the spread of the hot electrons in the target induces a lower strength for the RSA electrostatic field and thus reduces proton energies, whereas FSA is not affected. We observe that for thicknesses $>$85 μm, RSA protons are reduced to lower energies than the FSA ones.

These results are obtained as follows. We observe on films two proton beams accelerated at high laser intensity

($\sim$1–6 $\times$ 10^{19} W/cm^2) with distinct angular and energy distributions. To single out the properties of either FSA or RSA ions, we use a nuclear activation technique to measure deuterons accelerated from only one surface of the targets. The deuteron acceleration is affected by protons simultaneously accelerated from contaminant layers. Particle-in-cell (PIC) simulations that reproduce well the experimental results are used to assess this effect. Finally, we self-consistently couple the validated PIC simulations with direct measurements to quantitatively compare the properties of RSA and FSA protons.

The experiments were performed using the 100 TW laser at the Laboratoire pour l'Utilisation des Lasers Intenses (LULI), and the 30 TW Trident laser at the Los Alamos National Laboratory. Both produce pulses of $\sim$20–30 J of $\lambda_0 = 1.057\ \mu$m light. The pulse duration and focal spot FWHM are 320 fs/6 μm at LULI and 850 fs/20 μm at Trident, leading to peak intensities of 6×10^{19} W/cm^2 at LULI and 10^{19} W/cm^2 at Trident. Both systems have ASE $\leq 6 \times 10^{12}$ W cm^{-2}, producing a preformed plasma with exponential scale lengths of $\sim$30 μm up to $\sim 10^{20}$ cm^{-3} and $\sim$3 μm up to solid density, as measured at LULI by a 0.3 ps interferometric probe at 0.35 μm. Unless stated otherwise, targets are irradiated at normal incidence.

As shown in Fig. 1, two proton beams with distinct angular and energy distributions are observed to be accelerated from untreated thin Al solid targets irradiated at 6×10^{19} W/cm^2. The protons are detected in multiple layers of radiochromic film (RCF) densitometry media [16]. The RCFs used here are asymmetric [17], with their sensitive layer closest to the incident H$^+$ beam. The spatial distribution of the protons in a given RCF layer gives the angular emission pattern at a known interval of proton energy [2,6]. The first beam ("A"), collimated to a half-angle of $\sim$20°, penetrates in successive RCFs (only the first two are shown). The second beam ("B"), having a larger divergence than the first (>50°), appears only in the first RCF. Only beam A was observed when the RCFs in the stack were swapped so that the sensitive layer was further away from the incident H$^+$ beam. This implies that the widely spread beam B has a maximum energy (above the RCF detection threshold) <3 MeV. When the target was tilted, as shown in Fig. 1(d)–1(f), we observed that the centroid of both beams followed the target normal.

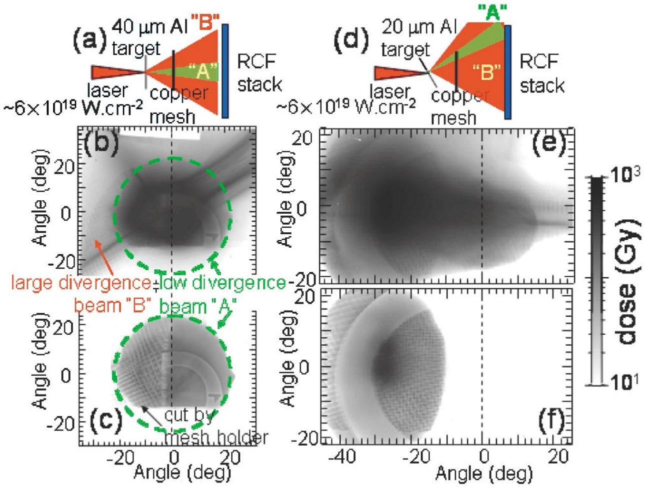

FIG. 1 (color). (a) Schematic of the experiment showing a double proton beam, (b) $\sim$2 MeV, and (c) $\sim$4.5 MeV RCF layers. (d)–(f) Same as (a)–(c) except that here the target is tilted by 30°. The observed structures in the proton beam are imprinted by the copper mesh.

2D PIC simulations performed in the conditions of the experiment shown in Fig. 1(d)–1(f) suggest that beam A (high-energy, low-divergence) is produced by RSA while beam B (low-energy, large-divergence) results from FSA. Similar observations were previously made using 3D PIC simulations [10]. To mock up the 3D configuration of the experiment in which the laser's linear polarization induces an anisotropy in hole boring and ion acceleration, we add the results of simulations made with P- and S-linear polarizations. Using 2D collisionless simulations for our experiments is valid since neither anomalous stopping induced by the low magnetic fields inside the target [18] nor collisions [18,19] do significantly influence the transport of the MeV electrons relevant to our case. The target substrate is a 20 μm thick slab of $40 \times n_c$ D$^+$ at an initial temperature of 1 keV [20]. The simulation box is 100 μm longitudinally and 20 μm transversally. The target rear surface is covered by a water vapor layer [H$^+$ (67%), O^{6+} (33%)]. The contaminant layer is estimated to be $\sim$2 nm thick [21]. To estimate the proportion of H$^+$ in the front side preformed plasma (whose scale length is modeled from the interferometric measurements), we suppose that H$^+$ and D$^+$ are homogenously mixed up to n_c. Such plasma corresponds to an ablated 2 nm of water vapor plus an additional ablated 62 nm of D$^+$. This implies a H$^+$ proportion in the plasma of $\sim$3%. Note that this maximizes the estimated concentration of H$^+$: if those were fully mixed with D$^+$ up to solid density (or if the H$^+$ would run in the front of the preformed plasma), the H$^+$ proportion could be as low as 0.03%. The simulation was run up to 1 ps, at which time acceleration of the high-energy ions ends. Lower energy ions will be produced over longer times as well as from wings of the laser pulse that are not accounted for in the simulations. This does, however, not affect our conclusions since we concentrate on the high-energy part (>2 MeV) of the ion spectra.

The FSA beam of Fig. 2, consistent with the observed beam B of Fig. 1, has a rapidly decreasing energy spectrum and a large divergence. FSA is expected to produce a large-divergence beam because the critical density (n_c) interface where the charge separation occurs is curved by the hole boring of the laser into the preplasma. The beam is centered along the target normal since the charge separation interface is compressed and tilted [22]. The RSA beam, consistent with beam A of Fig. 1, is well collimated, and clearly normal to the target rear surface with a slowly decreasing spectrum. Noticeably the high-energy portion of

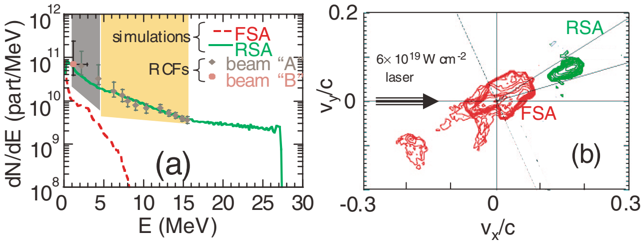

FIG. 2 (color). (a) Simulated angularly integrated H^+ spectra overlaid with the experimental spectrum (limited by the number of used RCF layers). The RCF sensitivities used are indicated in color. The RSA spectrum low-energy cutoff is due to H^+ contaminant depletion in the simulation. (b) Simulated phase space distribution of the FSA and RSA H^+ at $t = 400$ fs after the peak of the interaction. The target is tilted by 25 °. Each contour line corresponds to every $10^{0.3}$ of the ion number in a log scale.

the H^+ spectrum [Fig. 2(a)] shows a large predominance of RSA over FSA. We checked that, in the simulations, the FSA energy spectrum does not change significantly with a proton ratio below 10% since the sweeping acceleration [8] in the preplasma is dominated by the abundant species (D^+).

To confirm the prediction of the PIC simulations and the predominance of RSA over FSA for high-energy protons, we compare the simulations to measured deuterons accelerated selectively from a 0.5 μm thick CD_2 layer that we deposited *only* on one side of an Al foil. As in Ref. [13], the accelerated D^+ were discriminated from other ions by use of the $^{10}B(d, n)^{11}C$ nuclear reaction in a very high purity (99.82%) ^{10}B catcher foil [see Fig. 3(a)]. The catcher-activation technique is insensitive to other produced radiations (electrons or photons) and, as RCF, immune from saturation effects. After each shot, the catcher was placed between two NaI scintillation detectors to measure the ^{11}C beta-decay time series by the coincident detection of the 511 keV positron-annihilation quanta. The total ^{11}C yield was determined from the integral of the 20.38 min half-life decay curve, accounting for the shot time and the 30% detection efficiency (calibrated with ^{22}Na sources).

Figure 3(c) presents, for a laser intensity of 10^{19} W cm^{-2}, the measured ^{11}C yield for FSA D^+ (i.e., the CD_2 layer is deposited on the front of the target) and for different thicknesses of the Al substrate. For target thicknesses of 20 μm to 100 μm, we measure a rapid reduction of the ^{11}C activation yield, consistent with a slowing down of the FSA D^+ due to their passage through the substrate foil. Note that the FSA ions are unlikely to be influenced by the rear-surface sheath field since the PIC simulations show this field to be turned off when these slow ions cross the rear surface. For RSA D^+, we measure a 9×10^5 ^{11}C yield for a 20 μm target. Compared to Ref. [13], RSA D^+ acceleration is possible because we use thicker targets (with rear surfaces unperturbed by the ASE). The ^{11}C yield for RSA D^+ decreases with target thickness as the RSA field is reduced.

In order to relate the incident ion fluence on the catcher to the measured ^{11}C yield, we model the nuclear activation measurements by means of a Monte Carlo code. This code determines the angle-integrated ^{11}C yield in either a ^{10}B or ^{11}B catcher. It uses given D^+ and H^+ angularly resolved spectra and calculates in 3D the propagation of the particles through the foil and catcher (only for the ions generated in the ±48 ° acceptance of the catcher). It takes in account energy loss and angular scattering, both in the target and the catcher, using the code SRIM [23], and calculates the (d, n) or (p, n) reaction rate using their known cross sections [24].

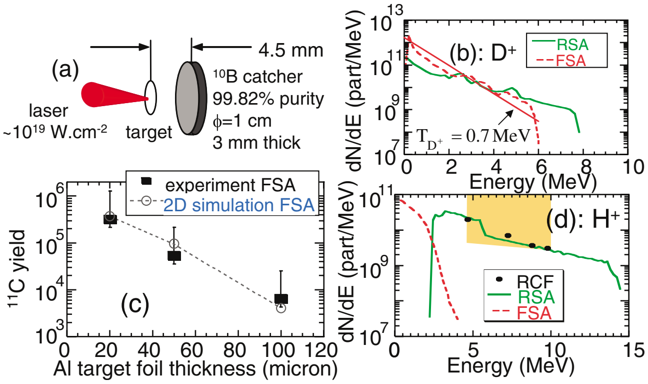

FIG. 3 (color). (a) Setup of the activation experiment at 10^{19} W cm^{-2}. (b) Simulated D^+ spectra for a 20 μm foil. The RSA D^+ have lower energy than if the H^+ layer would be absent since, due to their smaller mass, the H^+ are preferentially accelerated by RSA. (c) Experimental and simulated ^{11}C yield for FSA D^+. (d) Simulated H^+ spectra overlaid with the RCF inferred spectrum, both for a 20 μm foil. All spectra are angularly integrated.

A first approach to determine the spectrum of the FSA D^+ that matches the data of Fig. 3(c) is to use a Maxwellian spectrum with a high-energy cutoff [25]. The value of the cutoff proves to be very sensitive to fit the slope of the ^{11}C yield as a function of the Al substrate thickness. The best fit is obtained for $T_{D^+} = 0.7$ MeV and a cutoff of 6.1 MeV. As shown in Fig. 3(b), these values are in very good agreement with the FSA D^+ spectrum obtained from PIC simulations performed at 10^{19} W cm^{-2}, i.e., in the conditions of the experiment [26]. The PIC simulation spectrum also fits very well the experimental ^{11}C yield as a function of the substrate thickness, as shown in Fig. 3(c). Using the simulated RSA D^+ spectrum, we also get a good agreement between the experimental (9×10^5) and simulated (8.5×10^5) ^{11}C yield for the RSA D^+ for a 20 μm target.

The FSA H^+ cutoff is expected to be $\sim\frac{1}{2}$ of the D^+ one, i.e., ~3 MeV, since D^+ and H^+ have the same sweeping velocity [8], consistent with Fig. 3(b) versus Fig. 3(d). As the RCF evidence collimated high-energy H^+, at least up to 10 MeV [see Fig. 3(d)], these can be only RSA H^+, in agreement with the PIC simulation. This confirms the predominance of RSA over FSA at high ion energy. Quantitatively, we can assess that for a 20 μm thick target, the RSA H^+ beam contains 53 mJ above 3.5 MeV (56 mJ

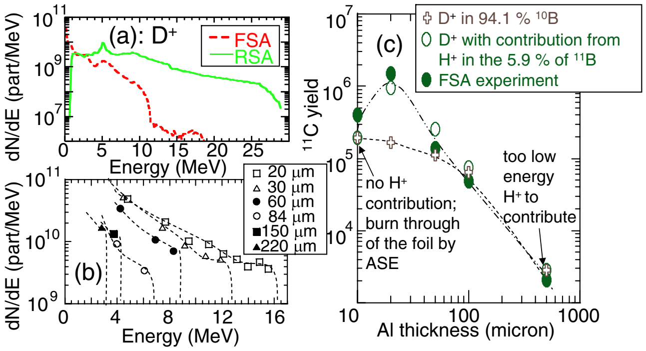

FIG. 4 (color online). Activation experiment at 6×10^{19} W cm^{-2}. (a) Simulated D^+ spectra for a 20 μm foil, (b) RCF inferred experimental H^+ spectra for different Al foil thicknesses (the lines are guides for the eye), (c) ^{11}C yield for FSA D^+, experimental (filled circles) and simulated with (empty circles) or without (crosses) the contribution from H^+ in ^{11}B inferred from the spectra shown in (b). All spectra are angularly integrated.

over all the spectrum, i.e., 0.3 % of the laser energy). Conversely, 25 μJ are, *at most*, contained in the front H^+ beam over the same range (12 mJ over the entire spectrum). Indeed, the energy in the FSA H^+ could be in reality much smaller since we deliberately maximized the proportion of H^+ in the front side preformed plasma.

Similar results are obtained when performing the experiment at higher intensity, namely 6×10^{19} W cm^{-2} (see Fig. 4). In this case the activation target was an isotopically enriched boron catcher (94.1% ^{10}B, 5.9% ^{11}B). The small admixture of ^{11}B caused some poisoning of the ^{11}C yield by the H^+ due to ^{11}B$(p, n)^{11}$C activation. The level of poisoning was experimentally assessed by measuring the H^+ spectra for various Al target thicknesses, as shown in Fig. 4(b). Note that we only need to assess the total H^+ spectrum for energies above 3 MeV since this is the reaction threshold for the ^{11}B$(p, n)^{11}$C reaction [27]. When taking in account the contribution of the H^+ and the simulated D^+ spectra [see Fig. 4(a)], we obtain a good agreement between the simulated and experimental ^{11}C yield for FSA D^+, as shown in Fig. 4(c). The total PIC-simulated H^+ spectrum compares well with that inferred from RCF, as shown in Fig. 2(a). At this intensity, we can assess that for a 20 μm thick target, the RSA H^+ beam carries 175 mJ in the experimentally observed 3.5–16 MeV range (275 mJ over all the simulated spectrum, i.e. ~1% of the laser energy). Conversely, 4 mJ are, *at most*, contained in the FSA H^+ beam over the same range (9 mJ over the entire spectrum). For thicker targets both mechanisms will produce lower energy protons because the RSA field is reduced and because FSA protons are slowed down in the target. For thickness ≤ 60 μm, since FSA protons are ≤ 7 MeV, RSA is still predominant, as attested by Fig. 4(b) which shows that higher proton energies are observed. For target thickness ≥ 85 μm, the proton energies observed in Fig. 4(b) become consistent with FSA H^+ slowed down in the target, hinting that FSA becomes then predominant.

The collimation of the predominant RSA H^+ is an important fact for potential applications such as table-top ion accelerators. FSA H^+ are limited to low energies (a few MeV) but could still be useful for future applications, such as radioisotope production, which do not require high quality beams. Finally we note that the PIC simulations show that relatively long pulses like ours (>300 fs) produce the highest energy H^+ whereas shorter pulses (e.g., 30 fs) have a higher conversion efficiency into ions.

We acknowledge the expert support of the LULI and Trident laser teams. This work was supported by Grant No. E1127 from Région Ile-de-France, EU program HPRI CT 1999-0052, LANL Laboratory Directed Research & Development, corporate support of General Atomics, and UNR Grant No. DE-FC08-01NV14050.

[1] E. Clark *et al.*, Phys. Rev. Lett. **84**, 670 (2000).
[2] R. A. Snavely *et al.*, Phys. Rev. Lett. **85**, 2945 (2000).
[3] T. Cowan *et al.*, Phys. Rev. Lett. **92**, 204801 (2004).
[4] M. Santala *et al.*, Appl. Phys. Lett. **78**, 19 (2001).
[5] M. Borghesi *et al.*, Phys. Plasmas **9**, 2214 (2002).
[6] M. Roth *et al.*, Phys. Rev. ST Accel. Beams **5**, 061002 (2002).
[7] P. Patel *et al.*, Phys. Rev. Lett. **91**, 125004 (2003).
[8] Y. Sentoku *et al.*, Phys. Plasmas **10**, 2009 (2003).
[9] M. Hegelich *et al.*, Phys. Rev. Lett. **89**, 085002 (2002).
[10] A. Pukhov, Phys. Rev. Lett. **86**, 3562 (2001).
[11] S. Karsch *et al.*, Phys. Rev. Lett. **91**, 015001 (2003).
[12] M. Zepf *et al.*, Phys. Rev. Lett. **90**, 064801 (2003).
[13] K. Nemoto *et al.*, Appl. Phys. Lett. **78**, 595 (2001).
[14] J. Fuchs *et al.*, Phys. Rev. Lett. **91**, 255002 (2003).
[15] A. Mackinnon *et al.*, Phys. Rev. Lett. **86**, 1769 (2001).
[16] N. V. Klassen *et al.*, Med. Phys. **24**, 1924 (1997).
[17] GAFCHROMIC® HD-810 Radiochromic Dosimetry Film and D-200 Pre-Formatted Dosimeters for High-Energy Photons, http://www.ispcorp.com/products/dosimetry/content/products/810_200/conspefo.html.
[18] Y. Sentoku *et al.*, Phys. Rev. Lett. **90**, 155001 (2003).
[19] A. Kemp *et al.*, Phys. Plasmas **11**, 5648 (2004).
[20] When the hydrogenous layer is directly on an Al target, FSA, driven by heavier ions, will occur at an even lower velocity [8]. RSA will not be significantly affected, which we confirmed by comparing the simulated RSA *E* fields for targets with $Z = 1$ or $Z = 10$.
[21] S. Gitomer *et al.*, Phys. Fluids **29**, 2679 (1986).
[22] H. Habara *et al.*, Phys. Plasmas **10**, 3712 (2003).
[23] J. F. Ziegler, J. P. Biersack, and U. Littmark, *The Stopping and Range of Ions in Solids* (Pergamon Press, New York, 1996).
[24] M. Firouzbakht, D. Schlyer, and A. Wolf, Nuclear Medicine and Biology **25**, 161 (1998).
[25] P. Mora, Phys. Rev. Lett. **90**, 185002 (2003).
[26] The target for this PIC simulation is modified so that, as in the experiment, it sits on the target rear surface a 0.5 μm CD_2 layer [i.e., D^+ (50%), C^{4+} (25%), C^{3+} (25%) [9]] covered by the same contaminants.
[27] R. E. Segel *et al.*, Phys. Rev. **139**, B818 (1965).